

The Salinity, Temperature, and $\delta^{18}\text{O}$ of the Glacial Deep Ocean

Jess F. Adkins,^{1*} Katherine McIntyre,¹ Daniel P. Schrag²

We use pore fluid measurements of the chloride concentration and the oxygen isotopic composition from Ocean Drilling Program cores to reconstruct salinity and temperature of the deep ocean during the Last Glacial Maximum (LGM). Our data show that the temperatures of the deep Pacific, Southern, and Atlantic oceans during the LGM were relatively homogeneous and within error of the freezing point of seawater at the ocean's surface. Our chloride data show that the glacial stratification was dominated by salinity variations, in contrast with the modern ocean, for which temperature plays a primary role. During the LGM the Southern Ocean contained the saltiest water in the deep ocean. This reversal of the modern salinity contrast between the North and South Atlantic implies that the freshwater budget at the poles must have been quite different. A strict conversion of mean salinity at the LGM to equivalent sea-level change yields a value in excess of 140 meters. However, the storage of fresh water in ice shelves and/or groundwater reserves implies that glacial salinity is a poor predictor of mean sea level.

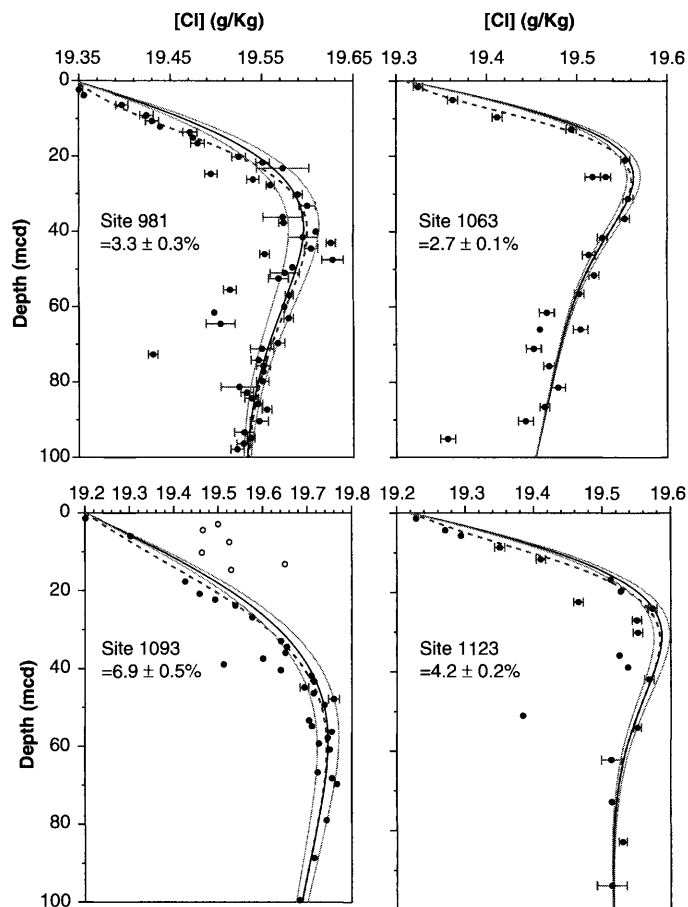
The general circulation of the modern deep ocean is dominated by two distinct water masses: In the Atlantic, warm, salty North Atlantic Deep Water (NADW) is formed north of Iceland and in the Labrador Sea, whereas in the Southern Ocean, cold, fresh Antarctic Bottom Water (AABW) forms on continental shelves. Because of its greater density, AABW underlies NADW in the Atlantic at all latitudes south of $\sim 40^\circ\text{N}$. No deep waters are formed in the North Indian or North Pacific Oceans today. The mean deep-ocean tracer properties are strongly weighted toward those of the Indo-Pacific abyss, where deep waters are roughly a 50/50 mixture of AABW and NADW (1) and the average overturning time is about 800 years (2).

Measurements of passive tracer fields (3–5) and the radiocarbon age difference between surface and deep waters (6–9) suggest that during the LGM the Atlantic was flooded by waters of a Southern Ocean origin, the LGM analog to NADW shoaled but still exited the Atlantic, and the mean overturning rate was somewhat slower than today. These changing patterns of deep tracer distributions are consistent over many glacial cycles (10).

Although these tracer distributions for the LGM have provided significant insight into the mechanisms of climate change, a better understanding of the deep circulation of the past requires constraints on the seawater density, a function of temperature, salinity, and

pressure. Oxygen isotope ratios ($\delta^{18}\text{O}$) within the carbonate shells of benthic foraminifera are a function of both temperature and sea-

Fig. 1. The top 100 m of pore-fluid [Cl] for four ODP sites and our model fits to the data. Solid lines are model results using the coral sea-level curve as the bottom-water [Cl] history. Dashed gray lines are a small alteration to this curve during the Holocene. There is more scatter in the [Cl] than the $\delta^{18}\text{O}$ because evaporation and fresh tap-water addition during squeezing have a much larger effect on the [Cl] values than on the $\delta^{18}\text{O}$ values. At site 1093, several of the points in the upper 20 m were rejected because they evaporated between sampling and measurement at Caltech. We are confident in ignoring these points because the shipboard [Cl] profile agrees with all of our points except these. Site 1123 has a wide scatter at the LGM peak and could be fit by a variety of other curves. The top boundary is constrained to match the local bottom-water value. This is a much stronger constraint for [Cl] than for $\delta^{18}\text{O}$ because the modern database of salinity values is so much larger than for oxygen isotopes. Our pore fluids are standardized to the same reference (IAPSO) as modern conductivity temperature-depth sensors. mcd, meters composite depth.



water isotopic composition, but distinguishing between these two effects is a long-standing problem in paleoceanography (11–13). A series of recent studies using pore fluids (14–16) and Mg/Ca ratios (17–19) have attempted to separate the temperature effect, but relatively little is known about the glacial salinity. Following a preliminary study in the North Atlantic (14), we used the pore-fluid approach (20, 21) to independently constrain the seawater salinity by using profiles of chlorinity from four Ocean Drilling Program (ODP) sites (Table 1). By combining these data with $\delta^{18}\text{O}$ measurements from the same locations (16), we have determined the spatial differences in salinity and temperature for the glacial deep ocean (22).

Sediment-pore water samples for these measurements were squeezed at sea and sealed in glass ampoules for transfer to our shore-based labs (23). Sample resolution varied between and within sites but ranged from every 1.5 m at site 981 to every 9 m at the bottom of site 1123 (Figs. 1 and 2). At all sites there is a pore-fluid maximum in $\delta^{18}\text{O}$ and [Cl] corresponding to the LGM ice-volume peak. If these systems were exactly analogous to diffusion in a pipe,

¹MS 100-23, Department of Geological and Planetary Sciences, California Institute of Technology, Pasadena, CA 91125, USA. ²Department of Earth and Planetary Sciences, Harvard University, Cambridge, MA 02138, USA.

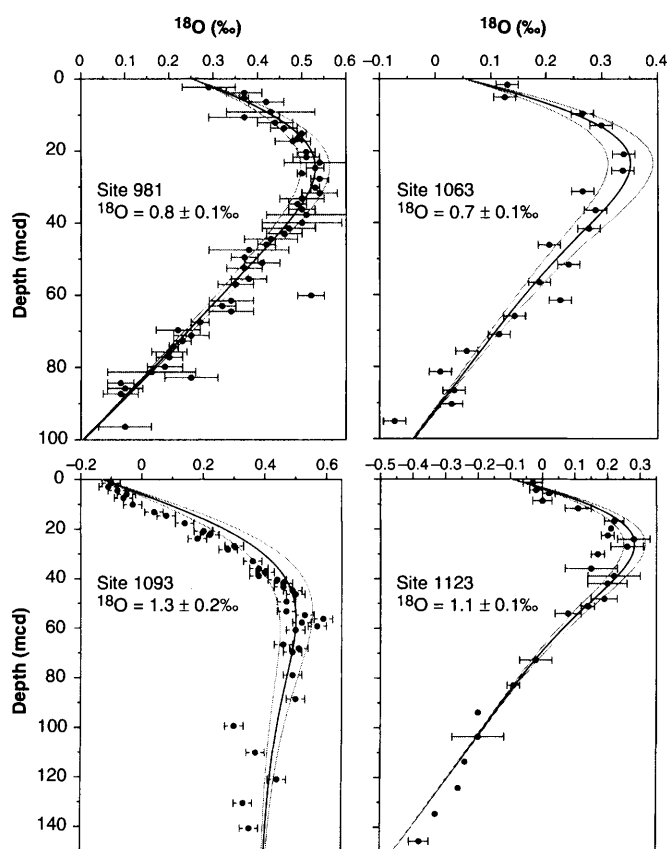
*To whom correspondence should be addressed. E-mail: jess@gps.caltech.edu

Table 1. Model-derived salinity, temperature, and $\delta^{18}\text{O}$ water for the four ODP sites at the LGM. Modern values were taken from GEOSECS data and checked against the Levitus database. LGM theta values were calculated by subtracting the reconstructed $\Delta\delta^{18}\text{O}$ water from the measured benthic $\delta^{18}\text{O}$ change and dividing this residual by 0.26‰/°C (57). This in situ temperature was converted to potential temperature with the use of standard conversion algorithms. LGM salinities are the product of the modern bottom water salinity and the model

derived % change from glacial to modern. [Cl] values are converted to salinity with the use of the standard factor of 1.80655. LGM $\delta^{18}\text{O}$ of seawater is the sum of the modern bottom-water value and the model-derived glacial-to-modern change. Error estimates for all modern values account for the local vertical gradient and the proximity of the site to nearby Geochemical Ocean Sections (GEOSECS) stations. LGM error bars are the propagated values of these modern estimates and the uncertainty from each model reconstruction.

Site information				Modern values				LGM values			
ODP site	Location	Lat.	Long.	Depth (meters)	Salinity (psu)	Theta (°C)	$\delta^{18}\text{O}$ water (‰)	Benthic change	Theta (°C)	Salinity (psu)	$\delta^{18}\text{O}$ water (‰)
1063	Bermuda Rise	33°41.1 81'N	57°36.9 03'W	4584	34.885 ±0.005	1.83 ± 0.01	0.05	1.9	-2.2 ±0.5	35.83 ±0.03	0.75 ±0.10
981	Feni Drift	55°28.6 32'N	14°39.0 48'W	2184	34.945 ±0.008	3.25 ± 0.05	0.25	2.0	-1.2 ±0.2	36.10 ±0.10	1.05 ±0.10
1123	Chatham Rise	41°47.1 60'S	171°29. 940'W	3290	34.730 ±0.005	1.30 ± 0.05	-0.10	1.7	-1.2 ±0.5	36.19 ±0.07	1.0 ±0.10
1093	Shona Rise	49°58.5 88'S	5°51.93 5'E	3626	34.685 ±0.003	0.35 ± 0.05	-0.20	1.6	-1.3 ±0.9	37.08 ±0.17	1.17 ±0.10

Fig. 2. The top 100 m of pore-fluid $\delta^{18}\text{O}$ for four ODP sites and our model fits to the data. Except for site 1123, these data have been reported previously. Model reconstructions are about 0.1‰ heavier than those in our earlier work due to the change in the bottom-water boundary condition's shape. Errors in our reconstruction represent 2σ estimates based on individual measurement errors and the scatter in the profile.



then we would expect the pore-fluid peaks in [Cl] and in $\delta^{18}\text{O}$ to be about 25 m below the sea floor. However, sediment accumulation over the last 20 thousand years (ky), compaction-driven advection, and the duration of the last glacial period all work to alter the actual depth. At our sites, the amplitudes from bottom-water minima to glacial maxima range from ~0.25 to 0.5 g/kg in chlorinity and 0.3 to 0.4 per mil (‰) in $\delta^{18}\text{O}$ (24). We measure [Cl] rather than salinity because the ratios of the major ions in

seawater are not constant with depth in the sediment column. Specifically, sulfate reduction and cation-clay interactions change the chemical composition of salinity. Chloride, outside of methane clathrate formation, is conservative in pore fluids and faithfully tracks the diffusively altered history of bottom-water salinity variations. Because of the separate bottom boundary conditions for the two species, slopes of [Cl] below the LGM peak tend to be less steep than those for $\delta^{18}\text{O}$. In several cases, the

[Cl] values begin to increase again below 100 m. Each of these sites is influenced by local volcanism, where the conversion of fresh ash to clay minerals removes water from the sediments, but this process does not affect significantly the upper part of the profile where porosity is larger and where there is more recent exchange with bottom waters (25).

The pore-fluid model (26) is forced with a time series of bottom-water [Cl] (or $\delta^{18}\text{O}$) for the last 125 ky. To construct this time series, we used a benthic foraminifera $\delta^{18}\text{O}$ record from Pacific core V19-30 (27) and the coral sea-level record for the last 30 ky (28–30). Because the benthic record contains effects due to both global ice volume and bottom-water temperature, we corrected the $\delta^{18}\text{O}$ record for temperature following Chappell and Shackleton (31). The results yield slight differences (~0.3‰ in salinity and ~0.1‰ in $\delta^{18}\text{O}$) from earlier work (14) for which such corrections were not made. The cumulative uncertainty in our pore-fluid reconstructions is smaller than the uncertainty in the glacial-interglacial change in $\delta^{18}\text{O}$ of benthic foraminifera used for the calculation of deep-ocean temperature.

Model fits to the chloride data are largely constrained by two parts of the profile, the LGM peak and the modern bottom-water value. Between these two points the model follows the history of sea-level change from glacial to modern (28–30) and the physics of diffusion. However, the fits in Fig. 1 consistently overestimate the [Cl] at a given depth for every site, similar to a problem identified for $\delta^{18}\text{O}$ profiles (16). Because we are calibrated to the same salinity scale as all of the modern hydrography measurements, our misfit must be due either to the imposed shape of the modern eustatic sea-level curve or to deep-water reorganizations during the Holocene, and not due to the wrong modern [Cl]. By gradually altering the sea-level curve over

Fig. 3. The modern and LGM temperature-versus-salinity relationships. The inset shows selected GEOSECS stations for all waters above a density of $48.0 \sigma_4$ and below a depth of 2500 m. Southern Ocean stations are shown in gray. The trends from the Southern Ocean into the three major basins are shown in black. Modern theta and salinity for each ODP site are shown as large circles. The main figure shows our estimates for LGM theta and salinity. The deep North Atlantic, the deep Pacific, and the deep Southern Ocean temperatures are all within error of the freezing point of seawater. The black arrow indicates the modern mean salinity. The LGM mean salinity for 125 m of eustatic sea-level change is shown by the bold arrow. Contour lines for the LGM data are isopycnals of σ_4 .

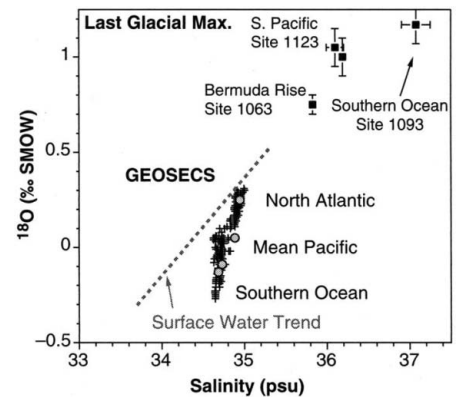
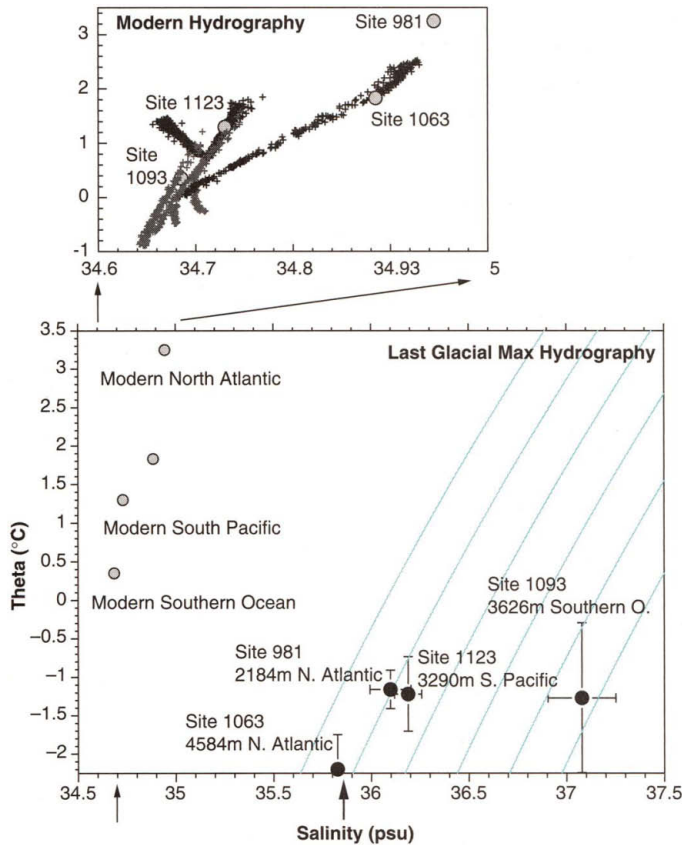


Fig. 4. The modern and LGM $\delta^{18}\text{O}$ -versus-salinity relationships. The mean modern $\delta^{18}\text{O}$ is by definition 0‰. The modern Southern Ocean deviates from the surface-water trend due to the combined effects of sea-ice formation and melting of the Antarctic Ice Sheet. The LGM data shows this same trend where site 1093 is much saltier but not much different in $\delta^{18}\text{O}$ from the other sites. These data support the interpretation that there was significant sea-ice formation in the Southern Ocean at the LGM.

the last 12,000 years to overshoot the modern sea level by several meters and then returning it to modern values in the last 1000 to 500 years, we can better fit the data (Fig. 1, gray lines). The choice of a sea-level curve to fit the upper portion of the data is somewhat arbitrary and requires further work. The required changes in the forcing function through the Holocene can be thought of as either a change in sea level over the mid-Holocene or a shift in the position of deep-ocean water masses. The latter explanation requires a shift in the opposite direction (i.e., toward fresher values) at other yet-undiscovered locations. In several sites, the same misfits are apparent for $\delta^{18}\text{O}$ (Fig. 2). However, the modern database for deep $\delta^{18}\text{O}$ is too sparse to rule out small misfits between our assumed bottom-water values and the true oceanic isotopic composition.

The modern and LGM temperature-versus-salinity diagram (Fig. 3) confirms that all deep waters are within error of the freezing point of seawater. The deep Pacific (site 1123), the Southern Ocean (site 1093), and the deep Atlantic (sites 981 and 1063) are all bathed in very cold waters. In contrast to the modern circulation, the bulk of the deep LGM ocean was relatively homogeneous in temperature. Temperature contrasts between separate source waters seen in the modern ocean were largely eliminated during the LGM. Site 1063 is colder and fresher than the

other areas. The LGM freezing point of surface seawater is -1.98°C , about 0.2°C warmer than our reconstructed value for the Bermuda Rise. Within the propagated error, our estimate for site 1063 does not violate the freezing point constraint, but the result may indicate that the low-resolution sampling of core 1063A has underestimated the glacial seawater $\delta^{18}\text{O}$ change.

Our salinity data also indicate that the modern deep Atlantic gradient of salty NADW and fresh AABW was reversed. At the LGM, the Southern Ocean was the saltiest water in the deep ocean by a large margin. This result places several important constraints on the mechanisms of deep-water formation. Today NADW is salty because of the influence of the Gulf Stream and North Atlantic Drift current system, which brings salty tropical waters from the Gulf of Mexico to the NADW formation region in the Greenland, Norwegian, and Iceland Seas (32). There is recent evidence that the Gulf Stream's flow through the Florida Strait was about two-thirds lower during the LGM as compared to the present (33). Coupled with about 3° to 5°C of tropical cooling (34, 35) and the associated decrease in evaporation, this decreased transport is an important part of the observed relative freshness of the glacial North Atlantic deep-circulation end member.

However, what is most notable about the northern salinity is its relative freshness compared to the Southern Ocean. Site 1093 is so

salty that a large imbalance in the freshwater budget must dominate the surface waters where this water mass is formed. The most likely mechanism for this imbalance is increased sea-ice formation and export (36). This mechanism is supported by our LGM $\delta^{18}\text{O}$ -versus-salinity reconstruction (Fig. 4). Modern hydrography shows that the Southern Ocean is anomalously salty relative to the surface-water trend for its $\delta^{18}\text{O}$ value (37). Sea-ice formation at and export from the sites of deep-water formation in the Southern Ocean preferentially fractionates salt by brine rejection but does not substantially change the water $\delta^{18}\text{O}$ (38). However, Toggweiler (39) has demonstrated that sea ice alone cannot explain the change in salinity from east to west across shelf waters before they slide off their western edges to feed new deep-water formation. He attributes half of the anomaly in the $\delta^{18}\text{O}$ signal to mixing with melt waters from the land-based Antarctic ice sheet, which are very fresh and extremely depleted in $\delta^{18}\text{O}$. Without surface data to constrain the LGM $\delta^{18}\text{O}$ -versus-salinity relationship, we cannot make the same sort of quantitative partitioning between sea ice and glacial melting. However, the data in Fig. 4 strongly support a large amount of sea-ice formation in the Southern Ocean. Although site 1093 has the highest salinity of the whole LGM deep ocean, it has similar $\delta^{18}\text{O}$ water value to most of the rest of the ocean. This signature of brine rejection without oxygen isotopic fraction is characteristic of sea-ice formation.

The presence of waters near the freezing point alters the balance of salinity and temperature's effect on seawater density (ρ), governed by the equation $\Delta\rho/\rho = \alpha\Delta T - \beta\Delta S$ (where ρ is density, T is temperature, and S is salinity). In

the modern ocean, where deep waters are on average 1° to 2°C potential temperature, the ratio of β , the haline contraction coefficient, to α , the thermal expansion coefficient, is about 10. Given the large temperature range of modern deep waters as compared to the modern salinity range, the modern $\Delta\rho$ is largely thermally controlled. For seawater near the freezing point, the β/α ratio rises to about 25. Density variations in the LGM deep were over two times more sensitive to salinity changes than they are today. Thus, the large expansion of the deep salinity gradient and the contraction of the thermal gradient at the LGM in our data are consistent with a much colder deep ocean. A first-order conclusion from our data is that the LGM thermohaline circulation was really more “haline” than “thermal,” with temperature setting the sensitivity of the system to salinity variations.

The salinity reconstructions (Fig. 3) at all sites are higher than 35.85 practical salinity unit (psu), the mean glacial value based on a 125-m eustatic sea-level change from Barbados corals (28) [this is 3.33% in the notation of Fig. 1 (40)]. Recent results from northern Australia (41), coupled with a global isostatic adjustment model, argue for 135 m of global eustatic sea-level change (42). In addition, the modern minimum Red Sea sill depth is 137 m, and this marginal basin seems to have remained in contact with the open ocean during the LGM (43). Therefore, 135 m of global sea-level change, corresponding to a mean ocean salinity of 35.95 psu, is a maximum estimate. With this global salinity constraint and our new data, we calculate a salt mass balance for the glacial ocean. On the basis of the data in Table 1, the glacial end members for northern- and southern-source deep waters are 35.83 and 36.15 psu, respectively. The southern end member is not the same value as site 1093 because this high-latitude source water must have mixed with fresher waters as it spread northward. With the use of Cd/Ca and $\delta^{13}\text{C}$ data to determine mixing ratios for the glacial Indian Ocean [50/50 northern/southern source mix (44)] and the glacial Atlantic Ocean [40/60 mix (45)], we calculated a mean Pacific salinity of 35.90 psu as a residual. This value is still lower than our measured salinity of 36.15 psu at site 1123 in the South Pacific. One possibility is that there is a mass of fresh water in the glacial ocean that we have not identified, possibly in the North Pacific.

Another explanation for our measurements is that they are consistent with 135 m of sea-level change and that $5 \times 10^6 \text{ km}^3$ of freshwater equivalent were sequestered without affecting sea level. Increases in both groundwater reserves and floating ice shelves at the LGM have the potential to account for this large amount of fresh water. Lowering sea level by 135 m exposes about 5% of the

current ocean area to the atmosphere. This new area and the depth of connected pore space below it represent a significant volume of water under the coastal ocean and continents that today contains salt but at the LGM contained fresh water. The net result is an increase in the glacial mean salinity that does not change sea level. We calculate a freshwater equivalent of $4.5 \times 10^6 \text{ km}^3$ for this fresh-salt water exchange (46). In the case of floating ice, adding the equivalent of about seven times the modern volume of Antarctic ice shelves (46) would balance the salinity budget. This is comparable to the increase proposed by Denton and Hughes (47). Although each of these freshwater reservoirs come close to solving the imbalance on their own, together the two make the uncertainty in glacial salinity distributions so large that the mean LGM salt concentration is not a good predictor of eustatic sea-level change.

References and Notes

1. S. Peacock, M. Visbeck, W. S. Broecker, in *Am. Geophys. Union Monograph. Inverse Methods Global Biogeochem. Cycles*, P. Kasibhatla et al., Eds. (American Geophysical Union, Washington DC, 2000), vol. 114.
2. M. Stuiver, P. M. Quay, H. G. Ostlund, *Science* **219**, 849 (1983).
3. J. C. Duplessy et al., *Paleoceanography* **3**, 343 (1988).
4. E. A. Boyle, *Annu. Rev. Earth Planet. Sci.* **20**, 245 (1992).
5. M. Sarnthein et al., *Paleoceanography* **9**, 209 (1994).
6. J.-C. Duplessy et al., *Radiocarbon* **31**, 493 (1989).
7. N. J. Shackleton et al., *Nature* **335**, 708 (1988).
8. W. S. Broecker, T. H. Peng, S. Trumbore, G. Bonani, W. Wolfli, *Global Biogeochem. Cycles* **4**, 103 (1990).
9. J. F. Adkins, E. A. Boyle, *Paleoceanography* **12**, 337 (1997).
10. M. E. Raymo, W. F. Ruddiman, N. J. Shackleton, D. W. Oppo, *Earth Planet. Sci. Lett.* **97**, 353 (1990).
11. W. Dansgaard, H. Tauber, *Science* **166**, 499 (1969).
12. R. G. Fairbanks, R. K. Matthews, *Quaternary Res.* **10**, 181 (1978).
13. N. J. Shackleton, *Nature* **215**, 15 (1967).
14. J. F. Adkins, D. P. Schrag, *Geophys. Res. Lett.* **28**, 771 (2001).
15. D. P. Schrag, G. Hampt, D. W. Murry, *Science* **272**, 1930 (1996).
16. D. P. Schrag et al., *Quaternary Sci. Rev.* **21**, 331 (2002).
17. Y. Rosenthal, G. P. Lohmann, K. C. Lohmann, R. M. Sherell, *Paleoceanography* **15**, 135 (2000).
18. D. W. Lea, D. K. Pak, H. J. Spero, *Science* **289**, 1719 (2000).
19. H. Elderfield, G. Ganssen, *Nature* **406**, 442 (2000).
20. D. P. Schrag, J. J. DePaolo, *Paleoceanography* **8**, 1 (1993).
21. H. Paul, S. Bernasconi, D. Schmid, J. McKenzie, *Earth Planet. Sci. Lett.* **192**, 1 (2001).
22. L. D. Labeyrie, J. C. Duplessy, P. L. Blanc, *Nature* **327**, 477 (1987).
23. J. M. Gieskes, T. Gamou, H. Brumsack, *ODP Technical Note* **15** (1991).
24. We measured the [Cl] of our pore fluids with the use of an automated potentiometric titration against a silver nitrate standard. The silver nitrate solution was standardized against International Association for Physical Science of the Ocean (IAPSO). Repeat measurements of a lab standard of surface ocean water were reproducible to $\pm 0.05\%$ at 2σ . Error bars reported in Fig. 1 are either the propagated error from weighing and volume-delivery uncertainty or the standard deviation of multiple replicates of the same sample. $\delta^{18}\text{O}$ values were determined as described in (15).
25. J. B. Martin, *Geochim. Cosmochim. Acta* **63**, 383 (1999).
26. The pore fluid model used to reconstruct the true changes at each site has been described previously (14, 16) but is briefly summarized below. Our 1-D diffusion scheme includes the effects of compaction advection but assumes there is no effect from externally forced advection through the sediment column. Fits are reported as a percentage of the increase over the modern bottom water for [Cl] and as the change in $\delta^{18}\text{O}$ from the modern value to the glacial maximum for oxygen (Figs. 1 and 2). Porosities and age models for each of the sites were taken from shipboard data as reported on the ODP Web site (www.oceandrilling.org). Our results are insensitive to relatively large variations in these two parameters. However, our results are sensitive to both the effective diffusion coefficient and the shape of the bottom-water boundary condition through time. Effective diffusion coefficients were found empirically by matching the depth of the LGM peak in the model profiles to the maxima in the data. This effective diffusivity is both temperature and tortuosity dependent, but it is not overly sensitive to either variable. Temperature profiles for each site are taken from down-hole measurements, and tortuosity is modeled as $1 - 2\ln(\phi)$ (48). Effective diffusion coefficients derived in this manner are independent of the size of the glacial-to-interglacial change in either tracer. This procedure of empirically matching to the data introduces about 20% variability in the effective diffusivity for both $\delta^{18}\text{O}$ and [Cl]. Our reconstructions include the contributions of this uncertainty in the reported errors.
27. N. J. Shackleton, J. Imbrie, M. A. Hall, *Earth Planet. Sci. Lett.* **65**, 233 (1983).
28. R. G. Fairbanks, *Nature* **342**, 637 (1989).
29. E. Bard, B. Hamelin, R. G. Fairbanks, *Nature* **346**, 456 (1990).
30. L. R. Edwards et al., *Science* **260**, 962 (1993).
31. J. Chappell, N. J. Shackleton, *Nature* **324**, 137 (1986).
32. V. Worthington, *Deep-Sea Res.* **17**, 77 (1970).
33. J. Lynch-Stieglitz, W. B. Curry, N. Slowey, *Nature* **402**, 644 (1999).
34. T. P. Guilderson, R. G. Fairbanks, J. L. Rubenstone, *Science* **263**, 663 (1994).
35. M. Stute et al., *Science* **269**, 379 (1995).
36. R. F. Keeling, B. B. Stephens, *Paleoceanography* **16**, 112 (2001).
37. W. S. Broecker, *Quaternary Res.* **26**, 121 (1986).
38. R. F. Weiss, H. G. Oestlund, H. Craig, *Deep-Sea Res.* **26**, 1093 (1979).
39. J. R. Toggweiler, B. Samuels, *J. Phys. Oceanog.* **25**, 1980 (1995).
40. Assuming the ocean basins have rectangular vertical sides with a mean depth of 3800 m means that a 125-m sea-level change corresponds to a salinity increase of 1.034 times (3.4%). However, the use of the true hypsometry of the modern ocean implies a 3.33% change for a sea level that is 125 m lower (35.85 psu for a modern mean salinity of 34.7 psu). The equivalent salinity change for a sea level that is 135 m lower is 35.95 psu.
41. Y. Yokoyama, K. Lambeck, P. De Deckker, P. Johnston, L. K. Fifield, *Nature* **406**, 713 (2000).
42. K. Lambeck, J. Chappell, *Science* **292**, 679 (2001).
43. E. J. Rohling et al., *Nature* **394**, 162 (1998).
44. E. A. Boyle, L. Labeyrie, J.-C. Duplessy, *Paleoceanography* **10**, 881 (1995).
45. J.-C. Duplessy et al., *Paleoceanography* **3**, 343 (1988).
46. Today coastal aquifers are constrained by a wedge of salty waters that range from ocean salinity at the sediment water interface to pure fresh water at a boundary under the continents that slopes away from the ocean with a value 40 times larger than the mean water table slope (49). Lowering the sea level 135 m shifts this wedge down the continental slope. The result is that the rectangular area between the modern and glacial wedges switches from relatively salty water today to fresh water at the LGM. This movement of water pushes extra salt into the glacial ocean without changing mean sea level. Multiplying the change in ocean area from today to the LGM (5% of the modern area) by the mean depth of interconnected pore space (assumed to be about 500 m), the mean porosity (0.5), and a factor of 0.5 for the mixture of fresh and saltwater implies a volume of $4.5 \times 10^6 \text{ km}^3$

of fresh water. This is enough to balance our measured salinity with a mean sea-level change of 135 m. Increases in ice-shelf volumes can also balance the salt budget. Given a total volume of $0.7 \times 10^6 \text{ km}^3$ for all the Antarctic ice shelves (50), there would have to be seven times this amount of floating ice at the LGM to balance our data with the sea-level constraints.

47. G. H. Denton, T. J. Hughes, in *The Last Great Ice Sheets*, G. H. Denton, T. J. Hughes, Eds. (Wiley, New York, 1981), pp. 437.

48. B. P. Boudreau, *Diagenetic Models and Their Implementation* (Springer-Verlag, Berlin, 1997).

49. P. A. Domenico, F.W. Schwartz, *Physical and Chemical Hydrology* (Wiley, New York, 1990).

50. D. J. Drewry, Ed., *Antarctica: Glaciological and Geophysical Folio*, sheets 2–9, Scott Polar Research Institute, University of Cambridge, Cambridge, UK (1983).

51. S.-T. Kim, J. R. O'Neil, *Geochem. Cosmochim. Acta* 61, 3461 (1997).

52. We thank K. Cuffey for insightful discussions about hydrology and E. Boyle and an anonymous reviewer for helpful comments. E. Boyle is thanked for inspiration and continued encouragement. E. Goddard provided assistance with lab work. Supported by NSF grant numbers OCE-0096814 to J.F.A. and OCE-0096909 to D.P.S.

17 July 2002; accepted 29 October 2002

Hybrid Speciation in Experimental Populations of Yeast

Duncan Greig,^{1,2} Edward J. Louis,³ Rhona H. Borts,³ Michael Travisano^{2*}

Most models of speciation require gradual change and geographic or ecological isolation for new species to arise. Homoploid hybrid speciation occurred readily between *Saccharomyces cerevisiae* and *Saccharomyces paradoxus*. Hybrids had high self-fertility (about 82%), low fertility when backcrossed to either parental species (about 7.5%), and vigorous growth under different thermal environments that favored one or the other of the parental species. Extensive karyotypic changes (tetrasomy) were observed in the hybrids, although genic incompatibilities accounted for 50% of the variation in self-fertility.

Speciation is thought to arise by gradual evolution of genic incompatibilities (1), ecological specialization (2, 3), or chromosomal differences (4) that prevent mating or cause inviable or infertile hybrid offspring (5). Rapid species formation can potentially occur by hybridization; however, the degree of reproductive isolation between potential new hybrid species and the two parental species is a major limiting factor. Hybrids must be self-fertile and sufficiently reproductively isolated to maintain a distinct lineage, but reproductive barriers between parental species must not preclude the initial hybridization. In postzygotically isolated species, where hybrids are typically inviable or sterile (6), these conflicting requirements can be achieved by a doubling of chromosome complement in the new species to produce an allotetraploid (7). Potentially, these requirements can also be met by maintaining chromosome number (homoploid hybrid speciation) (8, 9), but this mechanism is very uncommon in plants and unknown in animals (10).

Saccharomyces yeast species are postzygotically isolated, because hybrids form readily but are sterile, producing only ~1% viable gametes (spores) (11–13). However, populations of yeast can be very large ($>10^8$), and

viable gametes can be easily obtained. Moreover, the ability of *Saccharomyces* gametes to divide and switch mating type allows for autofertilization (gametophytic selfing) and, potentially, for instantaneous homoploid hybrid speciation. We investigated this potential with *Saccharomyces cerevisiae* and *Saccharomyces paradoxus* and measured the effects of intrinsic incompatibilities (hybrid sterility and infertility) and extrinsic incompatibilities (relative fitness of hybrids under different environmental conditions) (14).

First, we crossed *S. cerevisiae* and *S. paradoxus* and isolated 80 independent viable haploid gametes from their F_1 hybrid offspring. After allowing for spontaneous hybrid diploid formation by autofertilization (15), we found that 81.25% were capable of sporulation and that fertility (spore viability) was high (median = 90%; mean = 84.40%, with 95% confidence interval of 73.75 to 92.67%) (Fig. 1A) (15). Fertility was slightly reduced from that of the parental species (*S. cerevisiae*, 99.93%, 99.04 to 99.79%; *S. paradoxus*, 99.21%, 97.80 to 99.92%) (11), with statistically significant variation among F_2 hybrids ($F_{61,260} = 15.72$, $P < 0.0001$). We tested for reproductive isolation of the fertile F_2 hybrids from the parental species (Fig. 1B). The backcross hybrids have fertility that is significantly higher (7.54%, 5.38 to 10.02%) than that of F_1 hybrids (0.03%, 0.00 to 0.18%) (11), but they have fertility that is much lower than that of the F_2 hybrids ($F_{1,895} = 817.02$, $P \ll 0.0001$). Although rare, hybrid F_2 diploids are both fertile and isolated from their parental species.

Crossing F_2 hybrids and assessing fertility of their hybrid offspring demonstrated the existence of multiple different highly fertile F_2 hybrids (15). Ten independent F_2 genotypes, each having 100% fertility, were randomly paired and used to generate F_3 hybrids. All pairs yielded some viable gametes, but the average fertility of F_3 hybrids (10.64%, 0.93 to 28.97%) was much lower than that of their immediate parents; also, there was genetic variation in fertility among the F_3 hybrids caused by interaction between the F_2 parental genomes ($F_{4,94} = 5.65$, $P < 0.001$). Nevertheless, autofertilized F_4 hybrid diploids derived from the viable gametes had particularly high fertility (97.33%, 92.10 to

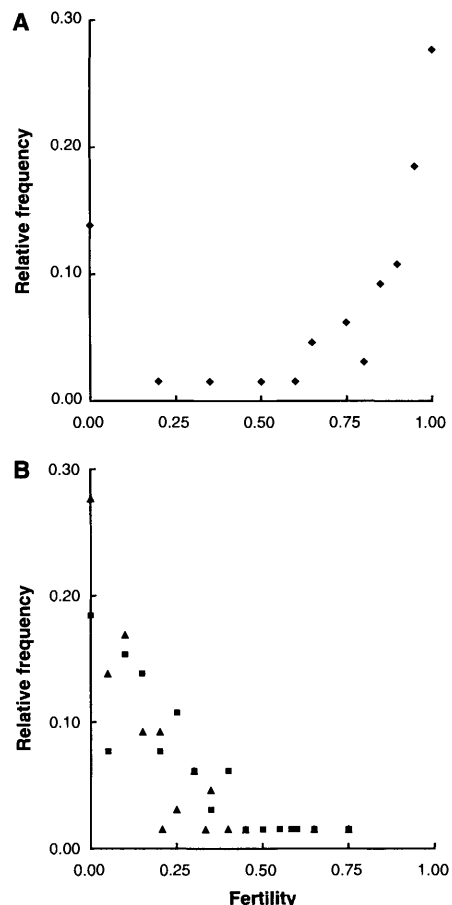


Fig. 1. Reproductive isolation of sporulation-proficient F_2 hybrids. (A) Hybrids have high fertility when crossed with themselves. (B) Hybrids have low fertility when crossed with either parental species (squares, *S. cerevisiae*; triangles, *S. paradoxus*).

¹The Galton Laboratory, Department of Biology, University College London, Gower Street, London WC1E 6BT, UK. ²Department of Biology, University of Houston, 4800 Calhoun Road, Houston, TX 77204, USA. ³Department of Genetics, University of Leicester, University Road, Leicester LE1 7RH, UK.

*To whom correspondence should be addressed. E-mail: mtrav@uh.edu